Itinerant and topological excitations in a honeycomb spiral spin liquid candidate

Yuqian Zhao[1,4], Xuping Yao [2,4], Xun Chen[1], Zongtang Wan[1], Zhaohua Ma[1], Xiaochen Hong[3] & Yuesheng Li [1] ✉

The frustrated insulating magnet can stabilize a spiral spin liquid, arising from cooperative fluctuations among a subextensively degenerate manifold of spiral configurations, with ground-state wave vectors forming a continuous contour or surface in reciprocal space. The atomic-mixing-free honeycomb antiferromagnet GdZnPO has recently emerged as a promising spiral spin-liquid candidate, hosting nontrivial topological excitations. Despite growing interest, the transport and topological properties of spiral spin liquids remain largely unexplored experimentally. Here, we report transport measurements on high-quality, electrically insulating GdZnPO single crystals. We observe a giant low-temperature magnetic thermal conductivity down to ~ 50 mK, described by $\kappa_{xx}^{\mathrm{m}} \sim \kappa_0 + \kappa_1 T$, where both κ_0 and κ_1 are positive constants associated with excitations along and off the spiral contour in reciprocal space, respectively. This behavior parallels the magnetic specific heat, underscoring the presence of mobile low-energy excitations intrinsic to the putative spiral spin liquid. Furthermore, the observed positive thermal Hall effect confirms the topological nature of at least some of these excitations. Our findings provide key insights into the itinerant and topological properties of low-lying spin excitations in the spiral spin-liquid candidate.

In strongly correlated magnets, frustration can give rise to exotic phases such as spin liquids, characterized by fractionalized excitations, long-range entanglements, and topological order[1,2]. These phases hold potential for applications in topological quantum computation[3], spintronics devices[4,5], and understanding high-temperature superconductivity[6]. Notably, some frustrated magnets with large spin quantum numbers (S) can stabilize spiral spin liquids (SSLs). The SSL emerges from cooperative fluctuations among subextensively degenerate spiral configurations, with ground-state wave vectors ($\mathbf{Q}_\mathrm{G}$) forming a continuous contour or surface in reciprocal space for two- (2D) or three-dimensional (3D) systems[7,8]. For instance, the SSL is predicted to stabilize in the easy-plane ($D \geq 0$) frustrated honeycomb-lattice model $\mathcal{H} = J_1 \sum_{\langle j0,j1 \rangle} \mathbf{S}_{j0} \cdot \mathbf{S}_{j1} + J_2 \sum_{\langle\langle j0,j2 \rangle\rangle} \mathbf{S}_{j0} \cdot \mathbf{S}_{j2} + D \sum_{j0} (S_{j0}^z)^2 - \mu_0 H g \mu_\mathrm{B} \sum_{j0} S_{j0}^z$, where J_1 and J_2 are the first- and second-nearest-neighbor Heisenberg couplings, H is the applied magnetic field along the z axis, and g is the g factor[9–14]. This SSL is predicted to remain stable down to very low temperatures[14], with $\mathbf{Q}_\mathrm{G}$ forming a continuous contour around the $\Gamma\{0, 0\}$ point for $1/2 > |J_2/J_1| > 1/6$, or around the K$\{1/3, 1/3\}$ point for $|J_2/J_1| > 1/2$.

Recently, the honeycomb antiferromagnet GdZnPO emerged as a promising candidate for realizing the above prototypical model experimentally (see Fig. 1), with $S = 7/2$, $J_1 \sim -0.39$ K, $J_2 \sim 0.57$ K, $D \sim 0.30$ K, and $g \sim 2$[15]. With $J_2/J_1 \sim -1.5$, $\mathbf{Q}_\mathrm{G}$ is expected to form a degenerate spiral contour around the K point below the crossover temperature $T^* \sim 2$ K, accompanied by low-energy topological excitations on the sublattices[15]. These excitations, including spin and momentum vortices, offer potential for applications in antiferromagnetic spintronics without magnetic field leakage[4,5], topologically protected memory and logic operations[16], fracton gauge theory[17–19], and beyond. Moreover, the spiral contour's approximate

[1]Wuhan National High Magnetic Field Center and School of Physics, Huazhong University of Science and Technology, Wuhan, China. [2]Kavli Institute for Theoretical Sciences, University of Chinese Academy of Sciences, Beijing, China. [3]Department of Applied Physics and Center of Quantum Materials and Devices, Chongqing University, Chongqing, China. [4]These authors contributed equally: Yuqian Zhao, Xuping Yao. ✉e-mail: yuesheng_li@hust.edu.cn
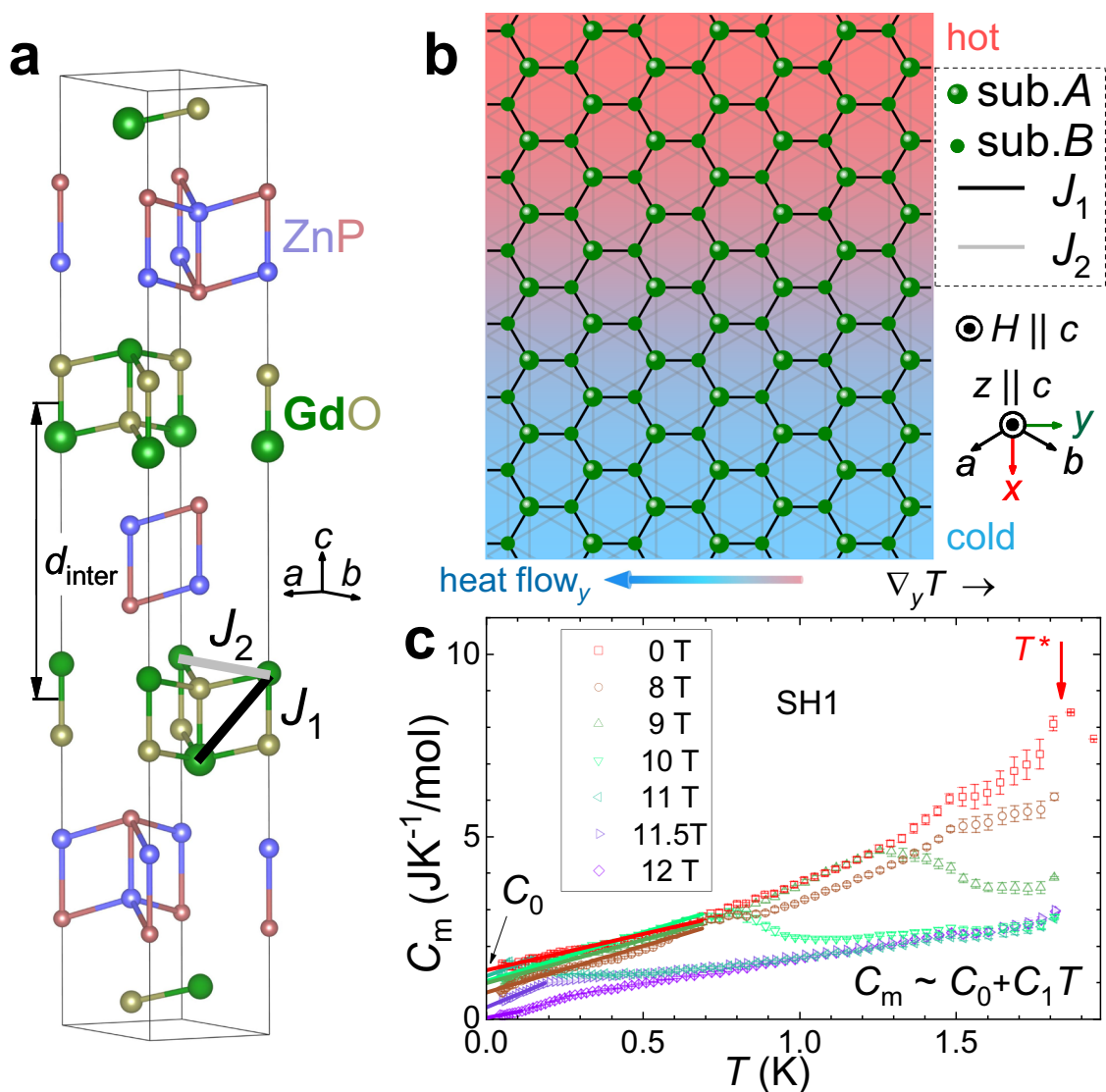
Fig. 1 | Lattice structure and magnetic specific heat of GdZnPO. a Crystal structure showing magnetic GdO layers separated by nonmagnetic ZnP layers, with an average interlayer distance $d_{inter} = c/3$ (-10.2 Å). The first- and second-nearest-neighbor exchanges J_1 and J_2 are indicated. Thin lines denote the unit cell. **b** Honeycomb lattice of Gd^{3+} ions. Inset: coordinate system for spin components and thermal transport. **c** Magnetic specific heat C_m of sample SH1 in selected magnetic fields ($\mu_0 H$) applied along the c axis. Colored lines are linear fits $C_m \sim C_0 + C_1 T$ below the temperature where C_m begins to exhibit linear behavior: below 0.7 K for $\mu_0 H < 11$ T, below 0.15 K at $\mu_0 H = 11$ T, below 0.2 K at $\mu_0 H = 11.5$ T, and below 0.12 K at $\mu_0 H = 12$ T. The fitted parameters C_0 and C_1 are shown in Fig. 3f. Crossover temperature T^* is marked, and error bars, 1σ s.e.

U(1) symmetry in momentum space[15,20] may enrich symmetry-breaking states, such as unidirectional spin-density waves[21], making SSLs promising platforms for exploring related phenomena like unidirectional pair-density waves. However, the transport and topological properties of SSLs remain largely unexplored experimentally.

The specific heat (C_m) of the generic 2D SSL is unusually large, following $C_m \sim C_0 + C_1 T$ at low temperatures, within the spherical approximation[7,8]. In the SSL, $\mathbf{Q}_G$ fluctuates along the continuous contour in reciprocal space, in sharp contrast to conventional magnetic states where $\mathbf{Q}_G$ adopts discrete values. Analogous to an ideal gas, this implies the presence of low-temperature spin degrees of freedom along the spiral contour, giving rise to a finite residual specific heat C_0. Therefore, C_0 arises from zero-energy excitations along the degenerate continuous contour in the classical limit ($S \rightarrow \infty$), while the $C_1 T$ term reflects low-energy excitations off the contour. To our knowledge, this low-T behavior of $C_m \sim C_0 + C_1 T$ had not been experimentally observed in any other compounds until our previous report on the SSL candidate GdZnPO[15]. In GdZnPO, measurements reveal

$C_0 = 0.9$–1.4 JK^{-1}/mol and $C_1 = 1.6$–3.4 JK^{-2}/mol below the crossover field $\mu_0 H_c \sim 12$ T, which separates the putative SSL and the polarized phase and is analytically given by $\mu_0 H_c = S[2D + 3J_1 + 9J_2 + J_1^2/(4J_2)]/(g\mu_B)$ in the classical limit (see Fig. 1c). These results support the stability of the honeycomb SSL down to at least ~ 50 mK. For $H \geq H_c$, the GdZnPO spin system becomes nearly fully polarized in a nondegenerate ferromagnetic phase. The field-induced transition from this ferromagnetic state ($H \geq H_c$) to the degenerate SSL ($H < H_c$) results in a significant entropy increase, decalescence, and a giant magnetocaloric effect–exceeding other known materials–underscoring GdZnPO's potential for magnetic cooling applications down to ~ 36 mK[22].

Despite extensive efforts[23–45], magnetic insulators with large thermal conductivity in the low-temperature limit remain exceptionally rare. GdZnPO single crystals are transparent insulators with no evident atomic-mixing disorder[15,46,47]. At low temperatures, the observed giant magnetic specific heat (C_m)[15] reflects a high density of low-energy spin excitations, which can lead to significant magnetic thermal conductivity $\kappa_{xx}^m \sim \frac{C_m \lambda_m \nu_m}{3 N_A V_0}$, provided the mean free path (λ_m)

and velocity (v_{m}) remain nonzero. Here, $V_0 = 67.6\,\text{Å}^3$ represents the volume per formula. Consequently, GdZnPO may serve as a rare example of an insulator that supports mobile unconventional spin excitations at low temperatures, offering an excellent platform for investigating the transport and topological properties of a 2D SSL candidate.

In this work, we conducted comprehensive transport measurements on five independent GdZnPO single-crystal samples. The sample with higher crystal quality exhibited reduced electric conductivity but enhanced thermal conductivity, indicating a nonzero intrinsic κ_{xx}^{m} in the low-temperature limit. At low temperatures, the behavior $\kappa_{xx}^{\mathrm{m}} \sim \kappa_1 T + \kappa_0$ is clearly observed in the highest-quality crystals. This behavior aligns well with the giant magnetic specific heat, $C_{\mathrm{m}} \sim C_1 T + C_0$, suggesting the presence of mobile, high-density spin excitations in GdZnPO. Additionally, a positive thermal Hall effect is observed, supporting the emergence of nonzero Chern numbers. Our findings suggest the itinerant and topological nature of low-lying excitations in the putative SSL, motivating further study.

Results

Toward intrinsic transport properties

Figure 1 a shows the crystal structure of GdZnPO[15,46,47]. The first-nearest-neighbor coupling, J_1 (with $|\text{Gd-Gd}|_1 \sim 3.7\,\text{Å}$), and the second-nearest-neighbor coupling, J_2 (with $|\text{Gd-Gd}|_2 = a \sim 3.9\,\text{Å}$), are mediated by Gd-O-Gd exchanges within the magnetic GdO layers. These magnetic layers are well separated by nonmagnetic ZnP layers, with an average interlayer distance of $d_{\mathrm{inter}} \sim 10.2\,\text{Å}$, indicating negligible interlayer coupling. The magnetic Gd^{3+} ions form a J_1-J_2 frustrated quasi-2D honeycomb lattice (Fig. 1b). Because of the zero orbital quantum number ($L = 0$) and negligible spin-orbit coupling of Gd^{3+}, interaction anisotropy, such as Dzyaloshinsky-Moriya (DM) anisotropy, is expected to be minimal. This is confirmed by the measured $g = 2.01(2)$[15], closely matching the free electron value ($g_{\mathrm{e}} = 2.0023$). The maximum DM interaction strength is estimated to be about $(|g - g_{\mathrm{e}}|/g_{\mathrm{e}}) J_2 \sim 1.4\% J_2$ ($\sim 0.01\,\text{K}$)[48] in GdZnPO.

Because thermal conductivity is highly sensitive to crystal quality, we first measured the low-temperature thermal conductivity of four randomly selected crystals (Supplementary Note 1 and Supplementary Figs. 1–6), followed by Laue x-ray diffraction (XRD) at 300 K and electrical resistivity below 300 K, to identify the intrinsic transport properties of GdZnPO. Fig. 2a shows the zero-field longitudinal thermal conductivity (κ_{xx}) data for samples TC1-TC4. The measured κ_{xx}/T vs. T curves are broadly similar across all investigated samples. However, sample TC4 exhibits a downturn below $\sim 0.3\,\text{K}$, contrasting with the behavior of the other samples. Such low-temperature suppression of κ_{xx}/T has also been reported in various magnetic systems, including $\text{PbCuTe}_2\text{O}_6$[42], YbMgGaO_4[27], $\text{Na}_2\text{Co}_2\text{TeO}_6$[25], and $\text{Cu}(\text{C}_6\text{H}_5\text{COO})_2\cdot 3\text{H}_2\text{O}$[43]. This phenomenon has been attributed to spin gap opening, many-body localization, and/or disorder effects that suppress the transport of spin excitations[25,27,42,43]. Laue XRD measurements were conducted to assess the crystallinity of each sample. Sample TC4 exhibits

significantly broader reflections than the other samples, as shown in Fig. 2c and the raw Laue XRD patterns in Supplementary Fig. 3, indicating a smaller average grain size. Crystal grain boundaries and other structural imperfections likely scatter quasi-particles, reducing their mean free path and thereby suppressing the thermal conductivity at low temperatures.

The electric resistivity (ρ_{xx}^{e}) data measured for the four samples are presented in Fig. 2b. As the temperature decreases below 300 K, ρ_{xx}^{e} ($\geq 300\,\Omega\text{m}$) increases, approximately following the Arrhenius law, $\rho_{xx}^{\mathrm{e}} = \rho_\infty^{\mathrm{e}} \exp(\Delta_{\mathrm{e}}/T)$, where ρ_∞^{e} and Δ_{e} denote the high-temperature resistivity limit and the thermally activated gap, respectively. Below $\sim 90\,\text{K}$ (for sample TC4) to 200 K (for sample TC3), the resistances (~ 0.7–$1.4\,\text{M}\Omega$ at 300 K) exceeded the measurement range ($\leq 6\,\text{M}\Omega$) of the physical property measurement system (PPMS). The gap Δ_{e} is roughly proportional to the low-temperature κ_{xx}/T, while inversely correlated with the full width at half maximum (FWHM) of Laue XRD reflections (see Fig. 2c). In insulating materials, crystal imperfections can introduce charge carriers and impair electrical insulation[44,49].

Consequently, higher-quality GdZnPO crystals with sharper Laue XRD reflections exhibit improved electrical insulation (with larger Δ_{e}) and enhanced low-temperature thermal conductivity. A similar trend has also been reported in the electrically insulating magnet $1T$-TaS_2[44]. These observations firmly establish the intrinsic low-temperature properties of GdZnPO: (1) electrical insulation and (2) the presence of itinerant magnetic excitations. Notably, the high-quality sample TC3 shows a large κ_{xx}/T value of $\sim 160\,\text{mWK}^{-2}\,\text{m}^{-1}$ at 70 mK and 0 T (the phonon contribution $\leq 6\,\text{mWK}^{-2}\,\text{m}^{-1}$ is negligible, see below), exceeding that of most other known electrically insulating magnets.

At low temperatures below 1 K, most of the thermal conductivity data across various measured fields can be well described by $\kappa_{xx} \sim \kappa_0 + \kappa_1 T + K_{\mathrm{p}} T^3$ (Supplementary Fig. 11). Here, the phonon prefactor K_{p} is given by $K_{\mathrm{p}} \sim \dfrac{4\pi^4 k_{\mathrm{B}} \lambda_{\mathrm{p}} v_{\mathrm{p}}}{5 Z V_0 \Theta_{\mathrm{D}}^3}$, where $v_{\mathrm{p}} = \dfrac{k_{\mathrm{B}} \Theta_{\mathrm{D}}}{\hbar} \left(\dfrac{Z V_0}{6\pi^2}\right)^{\frac{1}{3}}$ ($\sim 2900\,\text{m/s}$) represents the phonon mean velocity, $\Theta_{\mathrm{D}} \sim 117.5\,\text{K}$ is the Debye temperature determined from the specific heat of the nonmagnetic reference compound YZnPO (Supplementary Note 2 and Supplementary Fig. 16)[50,51], $Z = 6$ is the number of formulas per unit cell, and λ_{p} is the phonon mean free path. From the fitted values of $K_{\mathrm{p}} = 0.023, 0.052, 0.069$, and $0.066\,\text{WK}^{-4}\,\text{m}^{-1}$, we obtain $\lambda_{\mathrm{p}} \sim 4.8, 10.9, 14.5$, and $13.8\,\mu\text{m}$ for samples TC1-TC4, respectively—much smaller than the corresponding average sample width $W = 2\sqrt{A/\pi}$ ($\sim 251, 353, 252$, and $258\,\mu\text{m}$), where A denotes the cross-sectional area. Assuming $\lambda_{\mathrm{p}} = W$, the maximum phonon contribution to κ_{xx}/T is calculated as $K_{\mathrm{p}} T^2 \sim 6\,\text{mWK}^{-2}\,\text{m}^{-1}$ at $T = 70\,\text{mK}$ for sample TC3.

In practice, fitting low-T thermal conductivity data often yields a λ_{p} that is significantly smaller than W[33,42,52,53], as summarized in Supplementary Tab. 1. To our knowledge, there is no widely accepted explanation for this discrepancy. A natural speculation is that it arises from phonon scattering at grain boundaries or other imperfections that limit the phonon mean free path, despite the macroscopic sample dimensions. However, other studies—including our previous work on
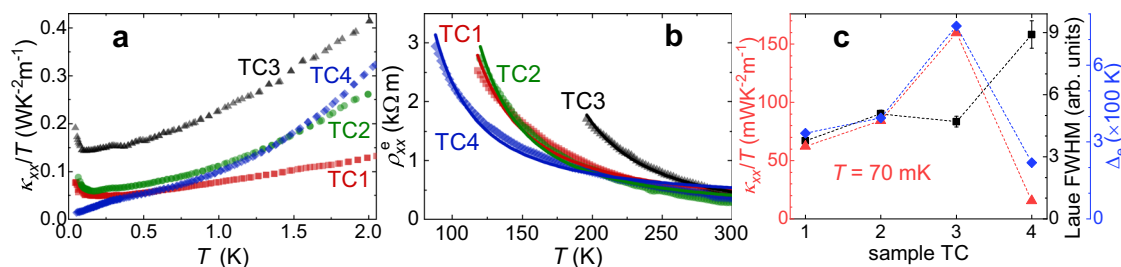

Fig. 2 | Sample dependence of transport properties measured on GdZnPO crystals. a Zero-field thermal conductivity (κ_{xx}) of four samples, plotted as κ_{xx}/T vs T, respectively. **b** Zero-field electrical resistivity (ρ_{xx}^{e}). Colored lines show Arrhenius-law fits, $\rho_{xx}^{\mathrm{e}} = \rho_\infty^{\mathrm{e}} \exp(\Delta_{\mathrm{e}}/T)$, with fitted gap values Δ_{e} shown in (**c**). **c** Sample dependence of κ_{xx}/T at 70 mK, average Laue x-ray diffraction full width at half maximum (Laue FWHM), and Δ_{e}. In **c**, error bars, 1σ s.e.
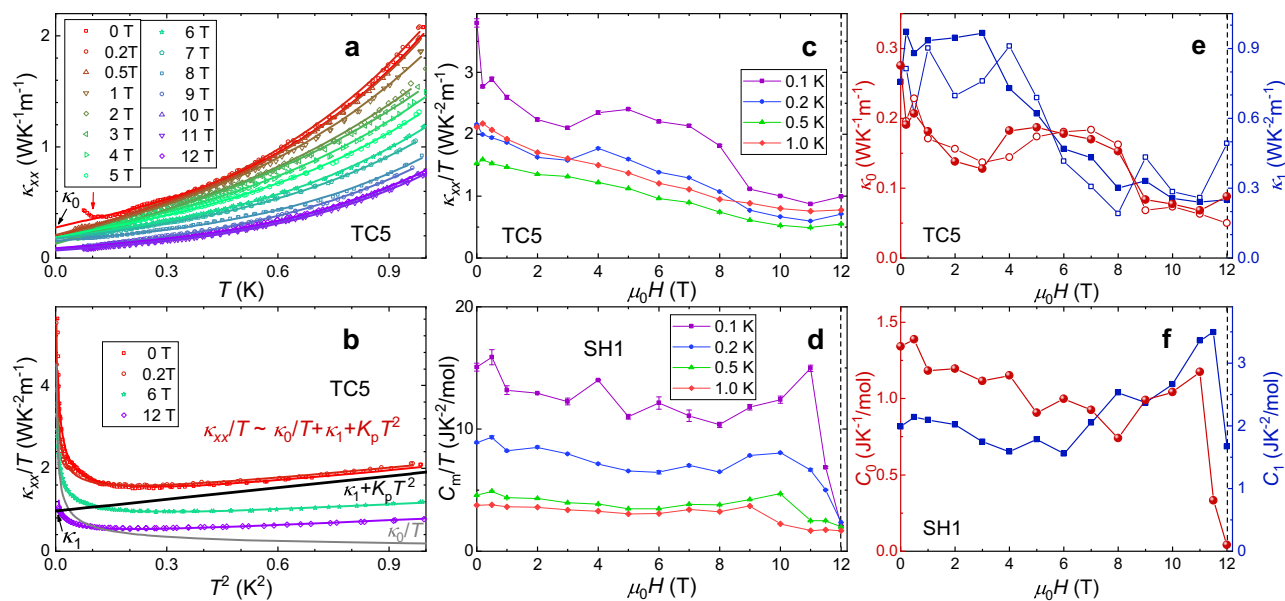
Fig. 3 | Thermal conductivity and specific heat of GdZnPO with magnetic field along the c axis. a Thermal conductivity κ_{xx} of sample TC5 at various fields, with fits $\kappa_{xx} \sim \kappa_0 + \kappa_1 T + K_p T^3$ below 1 K (colored lines). Fitted parameters κ_0 and κ_1 are shown in (**e**) (solid symbols). The vertical arrow marks the upturn onset in zero-field κ_{xx} as T decreases. **b** κ_{xx}/T vs T^2 for selected data. The gray and black lines represent the κ_0/T and $\kappa_1 + K_p T^2$ components, respectively, of the 0.2 T fit. **c, d** Field dependence of $\kappa_{xx}/$ T and magnetic specific heat C_m/T at selected temperatures (error bars: 1σ s.e.). **e, f** Field dependence of fitted parameters κ_0, κ_1, C_0, and C_1. In (**e**), open symbols show the fitted values of κ_0 and κ_1 from linear fits $\kappa_{xx} \sim \kappa_0 + \kappa_1 T$ at $T \leq 0.14$ K, where the $K_p T^3$ term (≤ 0.018 WK^{-1} m^{-1}) is negligible. Dashed lines in (**c–f**) mark the crossover field $\mu_0 H_c \sim 12$ T.

high-quality single crystals of α-CoV$_2$O$_6$ using a similar experimental setup[54]—have reported a λ_p comparable to W[55]. These suggest that the crystallinity of the randomly selected samples TC1-TC4 may simply have been insufficient. In the next section, we identify a higher-quality GdZnPO crystal, TC5, which exhibits sharp Laue photographs, improved electrical insulation, and significantly enhanced low-temperature thermal conductivity.

The average grain size may be roughly estimated from λ_p (≥ 4.8 μm), which is usually smaller than W, yet still more than four orders of magnitude larger than the lattice constant $a \sim 3.9$ Å. Theoretically, finite-size effects in thermodynamic properties become negligible when considering large spin clusters—on the order of $10^4 \times 10^4 \times 10^4$ sites. Therefore, no significant sample dependence is expected for the thermodynamic properties of our GdZnPO crystals. We have measured the low-temperature specific heat on two additional samples (SH1 and SH2) with different crystallinity qualities (Supplementary Fig. 9) to examine possible sample dependence. The specific heat shows negligible sample dependence, with $|C_m(\text{SH2})/C_m(\text{SH1}) - 1| \leq 0.1$ at 0 T, which falls well within the error margins of two independent ultra-low-temperature measurements. In contrast, thermal transport exhibits evident sample dependence—likely due to scattering from grain boundaries or other structural imperfections. For example, $\kappa_{xx}(\text{TC5})/\kappa_{xx}(\text{TC4}) - 1 \sim 20$–$350$ (Supplementary Fig. 10). This is reasonable given that $\kappa_{xx} \sim \frac{C\lambda v}{3N_A V_0}$, where λ is highly sensitive to sample crystallinity. Very similar sample dependence in both specific heat and thermal conductivity had been reported in several other frustrated magnets, including YbMgGaO$_4$[26,27,56,57] and Na$_2$BaCo(PO$_4$)$_2$[33,34].

Thermal conductivity of the highest-quality crystal

The thermal conductivity data of sample TC5 are expected to reflect the intrinsic properties of GdZnPO for the following reasons: (1) Sample TC5 exhibit sharp Laue photographs (Supplementary Fig. 9), and a room-temperature resistivity of $\rho_{xx}^e(300\text{ K}) \sim 11$ kΩm over 26 times higher than those of TC1-TC4 (~ 0.30–0.42 kΩm, see Fig. 2b). (2) In the case of GdZnPO, the low-temperature drop in κ_{xx}/T is mainly

observed in sample TC4 (see Fig. 2a), which exhibits broader Laue patterns and poorer electrical insulation (see above), suggesting that the suppression is caused by disorder effects. In contrast, sample TC5 shows no such drop. Instead, its thermal conductivity is well described by $\kappa_{xx} \sim \kappa_0 + \kappa_1 T + K_p T^3$ below 1 K, across various magnetic fields up to 12 T (see Fig. 3a, b). Remarkably, in zero field, sample TC5 even exhibits an unusual upturn in κ_{xx} below ~ 0.1 K, which is highly reproducible. This upturn is suppressed by a small magnetic field of ~ 0.2 T. A similar phenomenon was previously reported in the Kitaev material Na$_2$Co$_2$TeO$_6$, where the low-temperature rise in zero-field $\kappa_{xx}/$ T was attributed to the recovery of thermal transport by itinerant excitations at ultra-low temperatures[24]. (3) From the fits, we obtained a significantly enhanced $K_p \sim 0.94$ WK^{-4} m^{-1} (Fig. 3b), and $\lambda_p \sim 0.20$ mm, which closely matches $W = 0.21$ mm, for sample TC5. (4) As shown in Supplementary Fig. 12d, the fitted κ_0 first suddenly increases from nearly zero at 0 T to a large value at 0.5–0.6 T in samples TC1-TC3. Since C_0 is already significant at 0 T (see Fig. 3f) due to the putative SSL contour, we attribute this phenomenon to a disorder effect: the excitations along the spiral contour may be scattered by abnormal spin configurations near the grain boundaries, and a weak applied field of ~ 0.5 T may suppress this scattering caused by local perturbations from crystal imperfections. In the highest-quality sample TC5, this disorder effect is absent (see Fig. 3e), and the field dependence of κ_0 resembles that of C_0 (see Fig. 3f), except for the sudden drop of C_0 near the crossover field of ~ 12 T, which is discussed later.

The magnetic thermal conductivity, $\kappa_{xx}^m \sim \kappa_0 + \kappa_1 T$, is also significantly enhanced in the highest-quality sample TC5, with $\kappa_0 \sim 0.05$–0.28 WK^{-1} m^{-1} and $\kappa_1 \sim 0.25$–0.97 WK^{-2} m^{-1} across 0–12 T (see Fig. 3e and Supplementary Fig. 12). In conventionally condensed states, the specific heat (C) and thermal conductivity (κ_{xx}) of (quasi-)particles following Fermi-Dirac or Bose-Einstein statistics exhibit a low-temperature dependence of $\propto T^\beta$ or $\propto \exp(-\Delta/T)$, where $\beta \geq 1$ and $\Delta > 0$. Examples include $\beta = 1$ for fermionic systems, $\beta = 2$ for 2D antiferromagnetic bosonic systems, and $\Delta > 0$ for gapped systems. This behavior leads to either a finite constant or a vanishing C/T and κ_{xx}/T as $T \to 0$ K. Surprisingly, κ_{xx}/T measured on the highest-quality GdZnPO
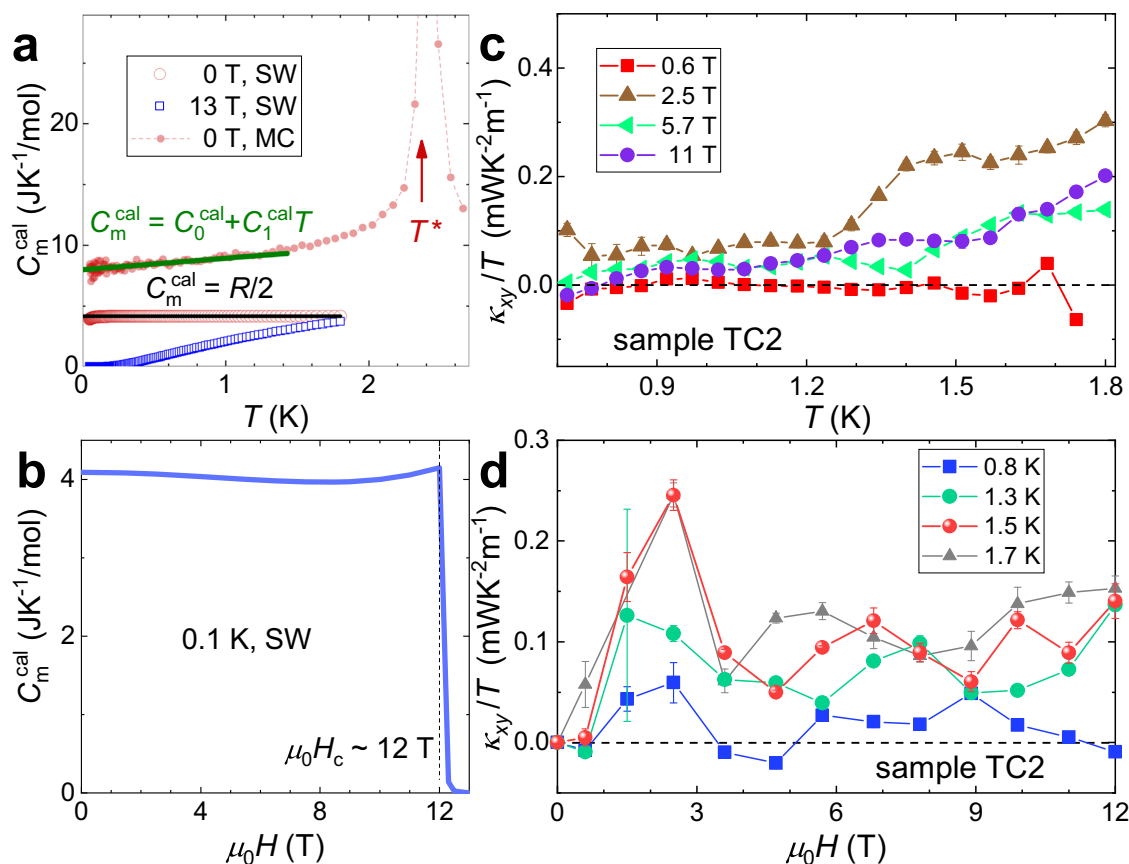
Fig. 4 | Calculated specific heat and thermal Hall conductivity (κ_{xy}) of GdZnPO sample TC2. a Specific heat (C_m^{cal}) calculated using spin-wave (SW) theory and Monte Carlo (MC) simulations. The black line represents the $C_m^{cal} = R/2$ behavior, while the olive line depicts a linear fit to the MC data using $C_m^{cal} = C_0^{cal} + C_1^{cal}T$. The crossover temperature T^* is indicated. **b** Field dependence of C_m^{cal} at 0.1 K. The dashed line marks the crossover field $\mu_0 H_c \sim 12$ T. **c** Temperature dependence of κ_{xy}/T at selected magnetic fields. **d** Magnetic field dependence of κ_{xy}/T measured at selected temperatures. In (**c, d**) error bars, 1σ s.e.

crystal TC5 exhibits a robust upturn, following $\kappa_{xx}/T \sim \kappa_0/T + \kappa_1 + K_p T^2$ below ~ 1 K (see Fig. 3b). Across fields up to 12 T, the magnetic thermal conductivity, $\kappa_{xx}^m \sim \kappa_0 + \kappa_1 T$, aligns with the magnetic specific heat behavior, $C_m \sim C_1 T + C_0$ (Fig. 1c), consistent with the relation $\kappa_{xx}^m \propto C_m$. For excitations along and off the putative SSL contour, we obtained $\lambda_{m0} v_{m0} \sim 3N_A V_0 \kappa_0/C_0 \sim$ 7.1–150 mm² s⁻¹, and $\lambda_{m1} v_{m1} \sim 3N_A V_0 \kappa_1/C_1 \sim$ 8.8–70 mm² s⁻¹ for sample TC5, depending on the applied magnetic field (see Supplementary Fig. 13)—values significantly smaller than the phonon parameter $\lambda_p v_p \sim 0.57$ m² s⁻¹. Using the mean magnon velocity calculated from spin-wave theory for spin excitations off the SSL contour, $v_{m1} \sim 110$ ms⁻¹ (Supplementary Note 3 and Supplementary Figs. 9, 10), we estimated $\lambda_{m1} \sim 0.5$ μm for the highest-quality sample TC5 at 0 T—a value more than three orders of magnitude larger than the lattice constant $a \sim 3.9$ Å, supporting the high mobility of low-energy spin excitations.

Along the SSL contour, the group velocity $v_{m0} \sim \nabla_{\mathbf{Q}_G} \omega$ (where $\hbar\omega$ is the excitation energy) is expected to be small due to ground-state degeneracy. However, weak quantum fluctuations from $S = 7/2$ and perturbations beyond the classical easy-plane frustrated honeycomb model may slightly lift this degeneracy, resulting in a nonzero v_{m0} in GdZnPO. This likely explains why the measured $\lambda_{m0} v_{m0}$ is nonzero.

At low temperatures, κ_{xx}/T decreases with increasing field and exhibits a broad hump around 6 T, while C_m/T remains nearly constant up to ~ 11 T before showing a sharp drop near the crossover field $\mu_0 H_c \sim 12$ T in agreement with spin-wave calculations (see Figs. 3c, d, 4b). Since the low-temperature (~ 0.1 K) heat transport is dominated by spin excitations along the spiral contour, the observed hump in κ_{xx}/T near 6 T and the drop in C_m/T near $\mu_0 H_c$ are mainly governed by the residual terms κ_0 and C_0, respectively (Fig. 3e, f). Within a quasiparticle

framework, the distinct field dependencies of κ_0 and C_0 arise from variations in the product $\lambda_{m0} v_{m0}$, which is generally field-dependent. Even at $\mu_0 H_c \sim 12$ T, the GdZnPO spin system is not fully polarized, as indicated by the measured susceptibility dM/dH remaining larger than the Van Vleck value ($\chi_{vv}^\parallel = 0.3$ cm³/mol)[15] at 50 mK (Supplementary Fig. 13), likely due to quantum fluctuations associated with the finite spin quantum number $S = 7/2$. As a result, both κ_0 and C_0 are significantly suppressed but remain finite at 12 T (see Fig. 3e, f and Supplementary Fig. 13c, d). The absence of a sharp drop in κ_0 suggests a sudden enhancement in the mean free path and/or group velocity of the excitations along the spiral contour, i.e., in $\lambda_{m0} v_{m0}$, likely driven by quantum fluctuations near $\mu_0 H_c$ (see Supplementary Fig. 13e). In contrast, the linear term κ_1 (Fig. 3e), and thus $\lambda_{m1} v_{m1}$, gradually decreases with increasing field up to 12 T, in rough agreement with the field dependence of the mean magnon velocity calculated for excitations off the SSL contour (see Supplementary Fig. 18c). While current models of magnetic thermal transport remain limited, the temperature and field dependence of C_m is qualitatively captured by spin-wave theory and Monte Carlo simulations (Fig. 4a, b).

Thermal Hall effect

The thermal Hall effect serves as a powerful probe of spin excitations[58–63]. Figure 4c presents the thermal Hall conductivity, κ_{xy}/T, measured on the high-quality GdZnPO sample TC2 with a magnetic field applied along the c axis. At ~ 1.5 K—well below the representative phonon Debye temperature $\Theta_D \sim 117.5$ K—a clear positive κ_{xy}/T is observed (Fig. 4c), and is expected to significantly exceed the phonon contribution[64]. Given that the Zeeman energy associated with ~ 12 T is only ~ 10 K, much smaller than the phonon energy scale (> 100 K), a
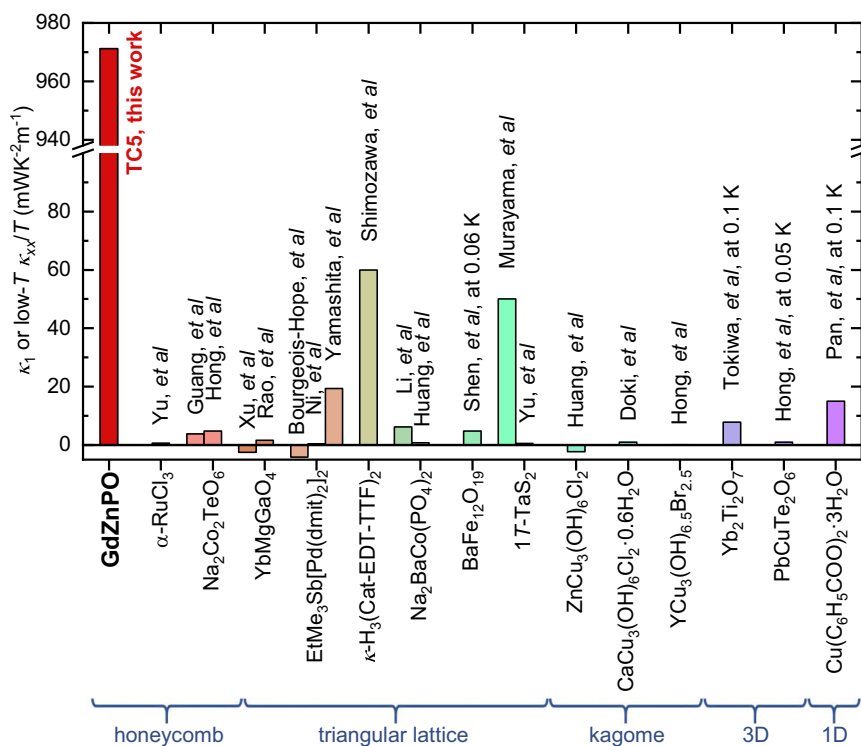
Fig. 5 | Low-temperature thermal conductivity, κ_1, of GdZnPO sample TC5 compared to other magnetic insulators. Previously reported κ_1 or low-temperature κ_{xx}/T values are shown for various magnetic insulators, including two-dimensional honeycomb α-RuCl$_3$[23] and Na$_2$Co$_2$TeO$_6$[24,25]; two-dimensional triangular-lattice YbMgGaO$_4$[26,27], EtMe$_3$Sb[Pd(dmit)$_2$]$_2$[29–31], κ-H$_3$(Cat-EDT-TTF)$_2$[32], Na$_2$BaCo(PO$_4$)$_2$[33,34], BaFe$_{12}$O$_{19}$[36], and 1T-TaS$_2$[44,45]; two-dimensional kagome ZnCu$_3$(OH)$_6$Cl$_2$[37], CaCu$_3$(OH)$_6$Cl$_2$·0.6H$_2$O[38], and YCu$_3$(OH)$_{6.5}$Br$_{2.5}$[39]; three-dimensional (3D) Yb$_2$Ti$_2$O$_7$[41] and PbCuTe$_2$O$_6$[42]; and one-dimensional (1D) anti-ferromagnetic Cu(C$_6$H$_5$COO)$_2$·3H$_2$O[43].

linear field dependence of the phonon thermal Hall conductivity, $\kappa_{xy}^p \sim a\mu_0 H$, is generally expected below 12 T within the linear response regime, where a is a constant[64–66]. Through a linear fit to the measured κ_{xy} between ~6 and 12 T, the estimated phonon contribution, $a\mu_0 H$, remains significantly smaller than κ_{xy} across the entire field range (see Supplementary Fig. 15c). Since GdZnPO is an insulator, the observed κ_{xy}/T is expected to predominantly arise from spin excitations. The residual value of observed κ_{xy}/T approaches zero below ~0.8 K (Fig. 4c), supporting a dominate bosonic origin[62,63]. On the honeycomb lattice, each unit cell contains two spins (see Fig. 1b), resulting in two bands. The temperature dependence of κ_{xy}/T can be approximated by the two-flat-band bosonic model[63], with the lower band's Chern number $C_s \sim 1$ (Supplementary Fig. 15a), supporting the topological nature of (at least some) spin excitations in GdZnPO.

As shown in Fig. 4d, κ_{xy}/T exhibits a peak at ~2.5 T, a feature strikingly similar to that recently observed in the SSL candidate MnSc$_2$S$_4$ at comparably low temperatures[67]. In that system, the peak has been attributed to a magnon thermal Hall effect arising from antiferromagnetic skyrmions at high fields. In GdZnPO, the classical easy-plane frustrated honeycomb model also supports spin and momentum vortices with nonzero winding numbers at finite fields[15], which may contribute to the observed thermal Hall effect (see Fig. 4c, d). Possible origins are further discussed in the next section. An oscillation-like feature in κ_{xy}/T appears at 1.5 K (see Fig. 4d), but no clear periodicity in $\mu_0 H$, $\mu_0^{-1} H^{-1}$[68], or $\log_{10}(\mu_0 H)$ is identified (see Supplementary Fig. 15). In addition, the pattern of κ_{xy}/T changes noticeably above ~4 T at a different temperature (see Fig. 4d), further suggesting that the apparent oscillations likely stem from ordinary measurement noise.

Discussion

The existence of nonzero magnetic thermal conductivity in the low-T limit, κ_1, remains a debated topic among various magnetic insulators,

including prominent spin-liquid candidates, as shown in Fig. 5[23–45]. The triangular-lattice spin-liquid candidate 1T-TaS$_2$ achieves a high reported value of $\kappa_1 \lesssim 50$ mWK^{-2} m^{-1}[44], though this remains a topic of debate[45]. Notably, 1T-TaS$_2$ exhibits a resistivity below 1 Ωm down to 0.5 K[44], over three orders of magnitude smaller than that of GdZnPO (Fig. 2b). Similarly, the spin-liquid candidate κ-H$_3$(Cat-EDT-TTF)$_2$ exhibits a comparably high value of $\kappa_1 \sim 60$ mWK^{-2} m^{-1}[32]. Consequently, GdZnPO emerges as a rare magnetic insulator with remarkably high intrinsic magnetic thermal conductivity, following $\kappa_{xx}^m \sim \kappa_1 T + \kappa_0$ in the low-T limit, with $\kappa_1 \sim 970$ mWK^{-2} m^{-1} (see Fig. 3b) and $\kappa_0 \sim 250$ mWK^{-1} m^{-1} (see Fig. 3a) at ~0 T from the highest-quality crystal TC5. The observed thermal conductivity in the low-T limit, κ_1, is exceptionally large compared to the other magnetic insulators (see Fig. 5). More importantly, the substantial residual thermal conductivity κ_0 (at ~0 T), attributed to spin excitations along the putative SSL contour in GdZnPO, has not been reported in other magnetic insulators to the best of our knowledge. These findings suggest the presence of intrinsic, mobile, high-density low-energy spin excitations and the stability of the putative SSL, without order by disorder, down to at least ~0.05 K in GdZnPO.

Because of the strong neutron absorption by Gd atoms, neutron scattering measurements on GdZnPO remain challenging. Nevertheless, several experimental observations support the emergence of an SSL in GdZnPO at low temperatures: (1) Low-temperature magnetization measurements clearly reveal easy-plane anisotropy. Combined with the crystal structure and magnetization data, the spin system of GdZnPO is well described by the $S = 7/2$ easy-plane J_1-J_2 honeycomb-lattice model[15]. Theoretically, an SSL is stabilized within this model across a broad parameter range, $|J_2/J_1| > 1/6$, persisting down to very low temperatures[14]. Furthermore, the experimentally determined Hamiltonian yields a crossover field of $\mu_0 H_c \sim 12$ T and a Curie-Weiss temperature of $\theta_w = -S(S+1)(J_1 + 2J_2) \sim -12$ K, both of which are in good

agreement with the experimental results on GdZnPO (see Fig. 3d, f)[15]. (2) Within the spherical approximation, the generic SSL theory predicts a low-temperature magnetic specific heat of $C_m \sim C_0 + C_1 T^8$—a distinctive behavior not reported in other spin systems to our knowledge. Experimentally, GdZnPO exhibits this feature at low temperatures up to the crossover field $\mu_0 H_c \sim 12$ T, see Fig. 1c. (3) Within the SSL ansatz on the honeycomb lattice, the zero-temperature susceptibility is theoretically predicted to be constant up to $\sim \mu_0 H_c$: $\chi_{cal}^{\parallel} = \mu_0 N_A g^2 \mu_B^2 / [2D + 3J_1 + 9J_2 + J_1^2/(4J_2)] + \chi_{vv}^{\parallel}$ (~ 4.4 cm³/mol), consistent with the experimental observations down to 50 mK ($\sim 0.4\% |\theta_w|$, see Supplementary Figs. 13a, 14a). (4) The giant magnetocaloric effect observed in GdZnPO is well explained by the determined easy-plane J_1-J_2 honeycomb-lattice spin Hamiltonian without tuning parameters[22]. (5) As shown in Fig. 3a, b, the temperature dependence of thermal conductivity closely follows the expected form $\kappa_{xx} = \kappa_0 + \kappa_1 T + K_p T^3$ below 1 K and up to the crossover field $\mu_0 H_c \sim 12$ T. Within the quasiparticle framework, the magnetic thermal conductivity is proportional to the magnetic specific heat, i.e., κ_{xx}^m ($\sim \kappa_0 + \kappa_1 T) \propto C_m$. Notably, the observation of a magnetic contribution $\kappa_{xx}^m \sim \kappa_0 + \kappa_1 T$ is highly distinctive and, to our knowledge, has not been reported in any other magnetic compound. This unusual thermal transport behavior further substantiates the emergence of an SSL in GdZnPO.

In the ordered phases of the pure easy-plane frustrated honeycomb model, linear spin-wave bands possess zero Chern numbers, implying no thermal Hall effect[11]. Thus, the positive thermal Hall effect observed in GdZnPO may stem from several factors: (1) The calculations[11] assume perfect SSL ground-state configurations, while low-energy topological excitations, like spin and momentum vortices, emerge at low temperatures[15], potentially yielding nonzero Chern numbers for the magnon bands via a fictitious magnetic flux[69]. These topological excitations may also contribute directly to the thermal Hall effect above ~ 1.2 K (Fig. 4c) through a momentum-transfer force[70] if they are mobile. (2) Weak perturbations, such as symmetrically allowed (Fig. 1a) DM interactions, may induce nonzero Chern numbers and a magnon thermal Hall effect[11]. (3) The low-energy structure of the spiral contour may accommodate other thermal excitations that contribute to thermal Hall transport. (4) While the calculations are classical[11], GdZnPO's $S = 7/2$ system exhibits weak quantum fluctuations.

The putative 2D SSL in the frustrated honeycomb-lattice antiferromagnet GdZnPO has been shown to persist from $T^* \sim 2$ K down to ~ 0.053 K, confirming its stability with a high density of low-energy spin excitations at $H < H_c$[15]. This work further demonstrates that these excitations are not only mobile but also at least partially topological, as evidenced by the observed giant low-temperature thermal conductivity (down to ~ 0.05 K) and positive thermal Hall effect. These findings provide new avenues for exploring the exotic transport and topological properties of low-lying excitations in SSL candidates.

Methods
GdZnPO single crystals were grown using the flux method[15]. Despite nearly identical synthesis procedures, the crystal sizes, Laue FWHMs, electric resistivities, and low-temperature thermal conductivities vary significantly between samples (see Fig. 2). In contrast, the low-temperature specific heat shows weak sample dependence across all three measured samples, as shown in Supplementary Fig. 10. The as-grown oxide single crystals of GdZnPO are very thin (thickness $\lesssim 0.1$ mm) and mechanically fragile. High-resolution measurements of both thermal conductivity and specific heat require relatively large crystals —with length $\gtrsim 1$ mm or mass $\gtrsim 1$ mg. Unfortunately, crystals often broke into smaller fragments during the careful removal of silver paste (used in thermal conductivity measurements) or GE varnish (used in specific heat measurements), making it impractical at present to measure both properties on the same GdZnPO crystal. Sample TC3 was

confirmed to have broken during the thermal-conductivity experiment at fields above ~ 6 T due to the torque induced by the easy-plane anisotropy of the spin system, and thus, we failed to collect its higher-field data.

The as-grown crystals' longest dimension aligns with the [110] direction, as determined by Laue XRD, and thermal or electrical currents were applied along this direction (Fig. 1b). Longitudinal thermal conductivity and thermal Hall conductivity were measured using standard four- and five-wire steady-state methods[54], respectively, in magnetic fields up to 12 T along the c axis and temperatures ranging from 0.05 to 2 K, achieved with a superconducting magnet and a ³He-⁴He dilution refrigerator (Supplementary Note 1 and Supplementary Figs. 1–12). We employed a cantilever-based thermal conductivity setup that was thermally isolated from all supporting components, with only minor additional heat flow occurring primarily through the NbTi superconducting leads (13 mm in length and 63 µm in diameter) connected to the heater and thermometers (Supplementary Fig. 7c). The resulting heat-leakage conductance is negligibly small, as detailed in Supplementary Note 1.

Specific heat down to 43 mK and magnetization down to 50 mK were also measured in the ³He-⁴He dilution refrigerator[15]. Crystal quality was accessed via the FWHM of Laue XRD reflections measured under identical conditions. Electrical resistance measurements were conducted using a PPMS (Quantum Design). Linear spin-wave theory was employed to simulate the specific heat and mean magnon velocity using the previously determined GdZnPO Hamiltonian[15], without parameter tuning (Supplementary Note 3 and Supplementary Figs. 17, 18). Standard MC simulations of the specific heat were performed on a 2×60^2 cluster with periodic boundary conditions, using the same Hamiltonian. Each simulation comprised 15,000 MC steps at each of 200 temperatures, annealing gradually from 50 K to 0.05 K, with 5000 steps allocated for thermalization.

Data availability
The data generated within the main text are provided in the Source Data. Additional raw data are available from the corresponding authors upon request.

References
1. Savary, L. & Balents, L. Quantum spin liquids: a review. *Rep. Prog. Phy.* **80**, 016502 (2016).
2. Zhou, Y., Kanoda, K. & Ng, T.-K. Quantum spin liquid states. *Rev. Mod. Phys.* **89**, 025003 (2017).
3. Nayak, C., Simon, S. H., Stern, A., Freedman, M. & Das Sarma, S. Non-Abelian anyons and topological quantum computation. *Rev. Mod. Phys.* **80**, 1083 (2008).
4. Jungwirth, T., Marti, X., Wadley, P. & Wunderlich, J. Antiferromagnetic spintronics. *Nat. Nanotechnol.* **11**, 231 (2016).
5. Gao, S. et al. Fractional antiferromagnetic skyrmion lattice induced by anisotropic couplings. *Nature* **586**, 37 (2020).
6. Lee, P. A., Nagaosa, N. & Wen, X.-G. Doping a Mott insulator: physics of high-temperature superconductivity. *Rev. Mod. Phys.* **78**, 17 (2006).
7. Bergman, D., Alicea, J., Gull, E., Trebst, S. & Balents, L. Order-by-disorder and spiral spin-liquid in frustrated diamond-lattice antiferromagnets. *Nat. Phys.* **3**, 487 (2007).
8. Yao, X.-P., Liu, J. Q., Huang, C.-J., Wang, X. & Chen, G. Generic spiral spin liquids. *Front. Phys.* **16**, 53303 (2021).
9. Mulder, A., Ganesh, R., Capriotti, L. & Paramekanti, A. Spiral order by disorder and lattice nematic order in a frustrated Heisenberg antiferromagnet on the honeycomb lattice. *Phys. Rev. B* **81**, 214419 (2010).
10. Owerre, S. A. Topological magnon bands and unconventional thermal Hall effect on the frustrated honeycomb and bilayer triangular lattice. *J. Phys.: Condens. Matter* **29**, 385801 (2017).

11. Fujiwara, K., Kitamura, S. & Morimoto, T. Thermal Hall responses in frustrated honeycomb spin systems. *Phys. Rev. B* **106**, 035113 (2022).

12. Okumura, S., Kawamura, H., Okubo, T. & Motome, Y. Novel spin-liquid states in the frustrated Heisenberg antiferromagnet on the honeycomb lattice. *J. Phys. Soc. Jpn.* **79**, 114705 (2010).

13. Shimokawa, T., Okubo, T. & Kawamura, H. Multiple-q states of the J_1 – J_2 classical honeycomb-lattice Heisenberg antiferromagnet under a magnetic field. *Phys. Rev. B* **100**, 224404 (2019).

14. Huang, C.-J., Liu, J. Q. & Chen, G. Spiral spin liquid behavior and persistent reciprocal kagome structure in frustrated van der Waals magnets and beyond. *Phys. Rev. Res.* **4**, 013121 (2022).

15. Wan, Z. et al. Spiral spin liquid in a frustrated honeycomb anti-ferromagnet: a single-crystal study of GdZnPO. *Phys. Rev. Lett.* **133**, 236704 (2024).

16. Yao, N. Y. et al. Topologically protected quantum state transfer in a chiral spin liquid. *Nat. Commun.* **4**, 1585 (2013).

17. Pretko, M. Subdimensional particle structure of higher rank U(1) spin liquids. *Phys. Rev. B* **95**, 115139 (2017).

18. Nandkishore, R. M. & Hermele, M. Fractons. *Annu. Rev. Condens. Matter Phys.* **10**, 295 (2019).

19. Pretko, M., Chen, X. & You, Y. Fracton phases of matter. *Int. J. Mod. Phys. A* **35**, 2030003 (2020).

20. Yan, H. & Reuther, J. Low-energy structure of spiral spin liquids. *Phys. Rev. Res.* **4**, 023175 (2022).

21. Hsieh, T.-C. & Radzihovsky, L. O(N) smectic σ model. *Phys. Rev. B* **108**, 224423 (2023).

22. Zhao, Y., Chen, X., Wan, Z., Ma, Z. & Li, Y. Giant magnetocaloric effect in a honeycomb-lattice spiral spin liquid candidate. *Adv. Sci.* e10086 (2025).

23. Yu, Y. J. et al. Ultralow-temperature thermal conductivity of the Kitaev honeycomb magnet α-RuCl$_3$ across the field-induced phase transition. *Phys. Rev. Lett.* **120**, 067202 (2018).

24. Guang, S. et al. Thermal transport of fractionalized anti-ferromagnetic and field-induced states in the Kitaev material Na$_2$Co$_2$TeO$_6$. *Phys. Rev. B* **107**, 184423 (2023).

25. Hong, X. et al. Phonon thermal transport shaped by strong spin-phonon scattering in a Kitaev material Na$_2$Co$_2$TeO$_6$. *npj Quantum Mater.* **9**, 18 (2024).

26. Xu, Y. et al. Absence of magnetic thermal conductivity in the quantum spin-liquid candidate YbMgGaO$_4$. *Phys. Rev. Lett.* **117**, 267202 (2016).

27. Rao, X. et al. Survival of itinerant excitations and quantum spin state transitions in YbMgGaO$_4$ with chemical disorder. *Nat. Commun.* **12**, 4949 (2021).

28. Yamashita, M. et al. Highly mobile gapless excitations in a two-dimensional candidate quantum spin liquid. *Science* **328**, 1246 (2010).

29. Bourgeois-Hope, P. et al. Thermal conductivity of the quantum spin liquid candidate EtMe$_3$Sb[Pd(dmit)$_2$]$_2$: No evidence of mobile gapless excitations. *Phys. Rev. X* **9**, 041051 (2019).

30. Ni, J. M. et al. Absence of magnetic thermal conductivity in the quantum spin-liquid candidate EtMe$_3$Sb[Pd(dmit)$_2$]$_2$. *Phys. Rev. Lett.* **123**, 247204 (2019).

31. Yamashita, M. et al. Presence and absence of itinerant gapless excitations in the quantum spin liquid candidate EtMe$_3$Sb[Pd(dmit)$_2$]$_2$. *Phys. Rev. B* **101**, 140407 (2020).

32. Shimozawa, M. et al. Quantum-disordered state of magnetic and electric dipoles in an organic Mott system. *Nat. Commun.* **8**, 1821 (2017).

33. Li, N. et al. Possible itinerant excitations and quantum spin state transitions in the effective spin-1/2 triangular-lattice antiferro-magnet Na$_2$BaCo(PO$_4$)$_2$. *Nat. Commun.* **11**, 4216 (2020).

34. Huang, Y. Y. et al. Thermal conductivity of triangular-lattice anti-ferromagnet Na$_2$BaCo(PO$_4$)$_2$: Absence of itinerant fermionic exci-tations. https://arxiv.org/abs/2206.08866 (2022).

35. Li, N. et al. Quantum spin state transitions in the spin-1 equilateral triangular lattice antiferromagnet Na$_2$BaNi(PO$_4$)$_2$. *Phys. Rev. B* **104**, 104403 (2021).

36. Shen, S.-P. et al. Quantum electric-dipole liquid on a triangular lattice. *Nat. Commun.* **7**, 10569 (2016).

37. Huang, Y. Y. et al. Heat transport in herbertsmithite: can a quantum spin liquid survive disorder? *Phys. Rev. Lett.* **127**, 267202 (2021).

38. Doki, H. et al. Spin thermal Hall conductivity of a kagome anti-ferromagnet. *Phys. Rev. Lett.* **121**, 097203 (2018).

39. Hong, X. et al. Heat transport of the kagome Heisenberg quantum spin liquid candidate YCu$_3$(OH)$_{6.5}$Br$_{2.5}$: Localized magnetic excita-tions and a putative spin gap. *Phys. Rev. B* **106**, L220406 (2022).

40. Jeon, S. et al. One-ninth magnetization plateau stabilized by spin entanglement in a kagome antiferromagnet. *Nat. Phys.* **20**, 435 (2024).

41. Tokiwa, Y. et al. Possible observation of highly itinerant quantum magnetic monopoles in the frustrated pyrochlore Yb$_2$Ti$_2$O$_7$. *Nat. Commun.* **7**, 10807 (2016).

42. Hong, X. et al. Spinon heat transport in the three-dimensional quantum magnet PbCuTe$_2$O$_6$. *Phys. Rev. Lett.* **131**, 256701 (2023).

43. Pan, B. Y. et al. Unambiguous experimental verification of linear-in-temperature spinon thermal conductivity in an antiferromagnetic Heisenberg chain. *Phys. Rev. Lett.* **129**, 167201 (2022).

44. Murayama, H. et al. Effect of quenched disorder on the quantum spin liquid state of the triangular-lattice antiferromagnet 1T-TaS$_2$. *Phys. Rev. Res.* **2**, 013099 (2020).

45. Yu, Y. J. et al. Heat transport study of the spin liquid candidate 1T-TaS$_2$. *Phys. Rev. B* **96**, 081111 (2017).

46. Nientiedt, A. T. & Jeitschko, W. Equiatomic quaternary rare earth element zinc pnictide oxides RZnPO and RZnAsO. *Inorg. Chem.* **37**, 386 (1998).

47. Lincke, H. et al. Magnetic, optical, and electronic properties of the phosphide oxides REZnPO (RE = Y, La-Nd, Sm, Gd, Dy, Ho). *Z. Anorg. Allg. Chem.* **634**, 1339 (2008).

48. Moriya, T. Anisotropic superexchange interaction and weak ferro-magnetism. *Phys. Rev.* **120**, 91 (1960).

49. Xiong, J. et al. High-field Shubnikov–de Haas oscillations in the topological insulator Bi$_2$Te$_2$Se. *Phys. Rev. B* **86**, 045314 (2012).

50. Liu, J. et al. Gapless spin liquid behavior in a kagome Heisenberg antiferromagnet with randomly distributed hexagons of alternate bonds. *Phys. Rev. B* **105**, 024418 (2022).

51. Liu, J. et al. Frustrated magnetism of the triangular-lattice antiferro-magnets α-CrOOH and α-CrOOD. *New J. Phys.* **23**, 033040 (2021).

52. Gofryk, K. et al. Anisotropic thermal conductivity in uranium diox-ide. *Nat. Commun.* **5**, 4551 (2014).

53. Hong, X. et al. Strongly scattered phonon heat transport of the can-didate Kitaev material Na$_2$Co$_2$TeO$_6$. *Phys. Rev. B* **104**, 144426 (2021).

54. Zhao, Y. et al. Quantum annealing of a frustrated magnet. *Nat. Commun.* **15**, 3495 (2024).

55. Toews, W. H. et al. Thermal conductivity of Ho$_2$Ti$_2$O$_7$ along the [111] direction. *Phys. Rev. Lett.* **110**, 217209 (2013).

56. Li, Y. et al. Gapless quantum spin liquid ground state in the two-dimensional spin-1/2 triangular antiferromagnet YbMgGaO$_4$. *Sci. Rep.* **5**, 16419 (2015).

57. Paddison, J. A. M. et al. Continuous excitations of the triangular-lattice quantum spin liquid YbMgGaO$_4$. *Nat. Phys.* **13**, 117 (2017).

58. Onose, Y. et al. Observation of the magnon Hall effect. *Science* **329**, 297 (2010).

59. Hirschberger, M., Krizan, J. W., Cava, R. J. & Ong, N. P. Large thermal Hall conductivity of neutral spin excitations in a frustrated quantum magnet. *Science* **348**, 106 (2015).

60. Katsura, H., Nagaosa, N. & Lee, P. A. Theory of the thermal Hall effect in quantum magnets. *Phys. Rev. Lett.* **104**, 066403 (2010).

61. Kasahara, Y. et al. Majorana quantization and half-integer thermal quantum Hall effect in a Kitaev spin liquid. *Nature* **559**, 227 (2018).

62. Yang, Y., Zhang, G. & Zhang, F. Universal behavior of the thermal Hall conductivity. *Phys. Rev. Lett.* **124**, 186602 (2020).
63. Czajka, P. et al. Planar thermal Hall effect of topological bosons in the Kitaev magnet α-RuCl$_3$. *Nat. Mater.* **22**, 36 (2023).
64. Li, X., Fauqué, B., Zhu, Z. & Behnia, K. Phonon thermal Hall effect in strontium titanate. *Phys. Rev. Lett.* **124**, 105901 (2020).
65. Strohm, C., Rikken, G. L. J. A. & Wyder, P. Phenomenological evidence for the phonon Hall effect. *Phys. Rev. Lett.* **95**, 155901 (2005).
66. Sugii, K. et al. Thermal Hall effect in a phonon-glass Ba$_3$CuSb$_2$O$_9$. *Phys. Rev. Lett.* **118**, 145902 (2017).
67. Takeda, H. et al. Magnon thermal Hall effect via emergent SU(3) flux on the antiferromagnetic skyrmion lattice. *Nat. Commun.* **15**, 566 (2024).
68. Zhang, D. et al. Large oscillatory thermal hall effect in kagome metals. *Nat. Commun.* **15**, 6224 (2024).
69. Mascot, E., Bedow, J., Graham, M., Rachel, S. & Morr, D. K. Topological superconductivity in skyrmion lattices. *npj Quantum Mater.* **6**, 6 (2021).
70. Schütte, C. & Garst, M. Magnon-skyrmion scattering in chiral magnets. *Phys. Rev. B* **90**, 094423 (2014).

Author contributions

Y.L. planned and supervised the project. Y.Z. and Y.L. collected the thermal transport, specific heat, Laue x-ray diffraction, and electrical resistance data. X.C., Z.W., and Z.M. prepared the GdZnPO single crystals. Y.L. and X.C. conducted the spin-wave calculations and Monte Carlo simulations. Y.L., Y.Z., X.Y., and X.H. analysed the data and wrote the manuscript with comments from all co-authors. The manuscript reflects the contributions of all authors.

Competing interests

The authors declare no competing interests.

Additional information

Supplementary information The online version contains supplementary material available at https://doi.org/10.1038/s41467-025-63620-x.

Correspondence and requests for materials should be addressed to Yuesheng Li.

Peer review information *Nature Communications* thanks Young Sun, Minoru Yamashita and the other anonymous reviewer(s) for their contribution to the peer review of this work. A peer review file is available.

Reprints and permissions information is available at http://www.nature.com/reprints

Publisher's note Springer Nature remains neutral with regard to jurisdictional claims in published maps and institutional affiliations.